University
of Glasgow

James Watt
School of
Engineering

FINAL YEAR PROJECT REPORT
BACHELOR OF ENGINEERING

Discovery of Cardiac Tissue Constitutive Behavior Using CANNs from Biaxial Testing Data

Thammatouch
Mutututharn

2937475M

2023-2024

Student Name: Thammatouch Mututharn	Student GUID: 2937475M
Course Code: ENG4110P	Course Name: INDIVIDUAL PROJECT 4
Name of 1st Supervisor: Ankush Aggarwal	Name of 2nd Supervisor: Thomas Franke
Title of Project: **Discovery of Cardiac Tissue Constitutive Behavior Using CANNs from Biaxial Testing Data**	

Declaration of Originality and Submission Information

I affirm that this submission is all my own work in accordance with the University of Glasgow Regulations and the School of Engineering requirements.

Abstract

Cardiac tissue exhibits complex anisotropic mechanical behavior that must be accurately characterized for predictive heart simulations in health and disease. This project aims to identify the constitutive behavior of myocardial tissue directly from biaxial mechanical testing data by using Constitutive Artificial Neural Networks (CANNs). Unlike traditional approaches that fit pre-selected strain-energy functions to data, CANNs learn the material law from experimental stress–strain observations, thus avoiding bias toward any assumed model form. We design a physics-informed neural network that encodes known biomechanical constraints (incompressibility, orthotropy, and material frame indifference) and train it on planar biaxial tension data of myocardium. The CANN autonomously discovers a sparse, interpretable constitutive model that best explains the tissue's nonlinear anisotropic response, overcoming the limitations of conventional, pre-defined models.

The resulting data-driven model consists of six invariant-based stress terms that accurately reproduce the biaxial behavior and reflect known cardiac microstructure. The CANN-derived law predicts tissue responses under loading conditions beyond the training set, including different stretch combinations, more reliably than fixed-form models. Moreover, the network's architecture yields physically meaningful parameters, addressing the interpretability challenge often encountered in neural network models.

Utilizing experimental biaxial testing data—where specimens were simultaneously stretched in two orthogonal directions (fiber and normal)—we considered five distinct loading conditions with varying fiber-to-normal stretch ratios: 1:1, 1:0.75, 0.75:1, 1:0.5, and 0.5:1. During these experiments, stretch (deformation) and the consequent normal (tensile) stress were recorded, allowing the networks to autonomously discern the intrinsic material behavior without relying on predefined mathematical models. Model discovery was regularized using L1-regularization to systematically promote sparsity in the parameter vector.

Remarkably, we have robustly derived a three-term model that incorporates a quadratic contribution of the fourth invariant, $I_{4,n}$, and exponential–quadratic contributions of the third and sixth invariants, $I_{4,f}$ and $I_{5,n}$. Crucially, this model is inherently interpretable and its parameters are expressed in well-defined physical units.

To assess the generalizability of our model, we further examined its performance on semilunar heart valve cusps, a related type of cardiovascular tissue. Specimens from porcine aortic and pulmonary semilunar heart valves were subjected to a similar biaxial loading protocol under seven distinct loading ratios, with the aim of determining if the model calibrated for human myocardial tissue could successfully capture the stress–strain behavior of semilunar heart valve cusps, thereby highlighting its robustness and transferability.

Acknowledgements

Contents

1 Introduction

Accurate modeling of myocardial mechanics is critically important for both biomedical research and clinical applications. The mechanical properties of the heart muscle determine how the cardiac chambers fill and eject blood, and thus influence overall cardiac function. Reliable constitutive models of myocardium are needed to simulate heart behavior in health and disease, with applications ranging from virtual surgical planning and medical device design to the study of cardiomyopathies (Fan and Sacks, 2014; Babaei et al., 2022). For example, patient-specific heart simulations can aid in treatment planning for heart failure or valve replacement, but their predictive power depends on having a realistic material law for cardiac tissue (Babaei et al., 2022). Consequently, constitutive modeling of soft cardiac tissue remains an active and challenging area of biomechanics research(Fan and Sacks, 2014).

Over the past several decades, many phenomenological and structurally-motivated constitutive laws have been proposed to capture the passive biomechanical behavior of heart muscle (Hadjicharalambous et al., 2014). Traditionally, myocardial tissue is treated as a pseudo-hyperelastic material and modeled using either phenomenological approaches (fitting generic mathematical functions to stress–strain data) or structural approaches (incorporating morphological features like muscle fiber orientation) (Fan and Sacks, 2014). A common phenomenological model is the Fung-type law, in which the strain energy is defined as a quadratic exponential function of strain (Fan and Sacks, 2014). Fung-type models (originating from the work of Y.C. Fung) have been widely used for soft tissues, including myocardium, because they can capture the pronounced nonlinearity of biological materials (Fan and Sacks, 2014). However, such models are purely empirical – their parameters lack direct physical interpretation, and they are generally unreliable outside the strain range for which they were calibrated (Fan and Sacks, 2014). Selecting the "best" model for a given dataset or application is typically left to expert judgment and convention, making the process subjective and prone to user bias (Martonová et al., 2024). Increasing a model's complexity to improve fit can also lead to over-parameterization: as the number of parameters grows, it becomes difficult to identify a unique set that fits the data, undermining predictive confidence (Hadjicharalambous et al., 2014).

To overcome these challenges, researchers have developed the concept of Constitutive Artificial Neural Networks (CANNs) – specialized neural network architectures that embed physical knowledge and constraints to ensure plausible material behavior Linka and Kuhl (2023). The key innovation of CANNs is to integrate century-old principles of material modeling into the learning algorithm, marrying data-driven flexibility with physics-based rigor Linka and Kuhl (2023). In a CANN approach, the network is structured to respect known symmetries and conservation laws: for example, inputs to the network can be chosen as strain invariants or other objective measures so that the network output automatically satisfies frame indifference Linka and Kuhl (2023). Likewise, the network can be designed to output a strain energy density (or a stress that derives from a potential), thereby enforcing thermodynamic consistency (material stability and energy conservation) by construction Linka and Kuhl (2023). Additional measures, such as custom activation functions and architecture constraints, can ensure that the learned response remains within physically reasonable bounds (e.g. avoiding negative stiffness, enforcing convexity of the strain energy) Linka and Kuhl (2023). By incorporating these domain-specific inductive biases, CANNs drastically reduce the risk of overfitting and improve extrapolation behavior, even when the experimental data are sparse Linka and Kuhl (2023). Another crucial feature of CANNs is that they can be formulated to be interpretable. Instead of arbitrary weight matrices, CANN frameworks often use a basis of known material functions or series expansions, such that the network's weights correspond to coefficients of interpretable stress contributions (Linka et al., 2023). The surviving terms in that case had clear physical interpretation, and the associated weights could be read as material stiffness parameters (Martonová et al., 2024; Linka et al., 2023). This ability to perform automatic feature selection—essentially picking out which mechanical aspects (invariants) are actually relevant to the material response—gives CANNs a high degree of interpretability and parsimony.

For our constitutive model of human myocardial tissue, we employ the constitutive-neural-network paradigm to let the network itself identify the most suitable formulation and parameter set from a broad space of candidate terms (Linka et al., 2021; Linka and Kuhl, 2023). Specifically, we construct a transversely

isotropic, perfectly incompressible CoNN that ingests the two isotropic invariants I_1 and I_2 together with the four anisotropic invariants I_{4f}, I_{4n}, I_{5f}, I_{5n}, and I_{8fn}, and returns an approximation of the strain–energy (free-energy) density. The architecture contains two hidden layers. First hidden layer: Generates the first power ($\circ$) and the squared power ($\circ$)^2 of every invariant. Second hidden layer: Applies both the identity ($\circ$) and the exponential $\exp(\circ)$ functions to each of the quantities produced by the first layer (Holthusen et al., 2023; Linka et al., 2023; Taç et al., 2024).

This configuration yields $6 + 8 + 16 = 30$ candidate basis terms, 16 trainable coefficients, and therefore $2^{16} = 65{,}536$ distinct model combinations. To pinpoint the optimal model within this set, we train the network on biaxial extension data obtained from human myocardial tissue (Sommer et al., 2015). Conceptually, we anticipate that training will drive many weights to zero, producing a comparatively dense but interpretable parameter vector (Peng et al., 2021). Intuitively, retaining more non-zero coefficients increases model complexity and can improve fidelity to the calibration data; nonetheless, overly rich formulations become less transparent and tend to generalize poorly to new loading scenarios (Alber et al., 2019; Nikolov et al., 2022; Brunton et al., 2016). To encourage sparsity, we augment the CANNs loss with an L_1-regularization (lasso) term—that is, the weighted sum of all network coefficients—so that the optimizer simultaneously penalizes model complexity (Frank and Friedman, 1993; McCulloch et al., 2024). By tuning the penalty weight α, we can control how many parameters remain non-zero: larger α values force additional coefficients to zero, whereas smaller values favor a lower data-misfit but a denser model. Consequently, α acts as a continuous dial between minimizing prediction error and minimizing the cardinality of the basis (Pierre et al., 2023; Flaschel et al., 2021). Because the optimal solution is highly sensitive to this hyperparameter and no universal rule exists for choosing it, identifying a suitable α becomes a central challenge in data-driven model discovery (McCulloch et al., 2024).

Accordingly, the aim of this study is to determine the constitutive form and parameter set that most faithfully capture the mechanics of human myocardial tissue by combining the CANNs framework with L_1-regularization. The manuscript is organized as follows: Sections 2.1 and 2.2 present a critical survey of the published biaxial-extension experiments that constitute our calibration data set. Section 2.3 recapitulates the essential continuum-mechanics background required for formulating hyperelastic models. Section 2.4 fuses these concepts into a new class of incompressible, orthotropic CANNs. Sections 3.1–3.3 report the outcomes of the model-discovery process under biaxial loading, while Section 3.4 extends the evaluation to porcine semilunar valve cusps to assess generalizability (Hudson et al., 2022). Section 4 discusses the implications of the findings, outlines limitations, and sketches directions for future research, followed by a concise conclusion.

2 Methods

This section begins with an overview of the published experimental mechanical biaxial extension data used to train the neural networks. We describe the constitutive equations considered, including the deformation gradient and its invariants, which serve as the foundation for the total strain energy density function at the heart of a constitutive artificial neural network.

2.1 Experimental dataset (Human Myocardial Tissue)

The constitutive neural network is trained using experimental data obtained from biaxial extension tests on human myocardial tissue, modeled as a transversely isotropic and perfectly incompressible material (Sommer et al., 2015). Square tissue specimens with dimensions $25 \times 25 \times 2.3 \, \text{mm}^3$ were subjected to biaxial stretching in fiber (f) and normal (n) directions Sommer et al. (2015). The applied stretch ratios included $1:1$, $1:0.75$, $0.75:1$, $1:0.5$, and $0.5:1$, generating five pairs of stretch-stress datasets. Table 1 summarizes the digitized experimental data, encompassing five biaxial extension tests (Sommer et al., 2015).

The deformation gradient F and Cauchy stress σ are structured with subscripts f and n, corresponding to the fiber and normal directions. The framework adheres to the incompressibility constraint ($J = 1$) and assumes transverse isotropy, aligning with the myocardium's microstructural anisotropy.

Table 1: **Biaxial extension data** form human myocardium recorded during biaxial extension tests on square human-myocardial specimens in two orthogonal directions at five different stretch ratios. Indices f and n denote the fiber direction and the normal direction, respectively. (Sommer et al., 2015)

λ [-]	$\lambda_f = \lambda$ $\lambda_n = \lambda$		$\lambda_f = \lambda$ $\lambda_n = 0.75\lambda$		$\lambda_f = 0.75\lambda$ $\lambda_n = \lambda$		$\lambda_f = \lambda$ $\lambda_n = 0.5\lambda$		$\lambda_f = 0.5\lambda$ $\lambda_n = \lambda$	
	σ_{ff} [kPa]	σ_{nn} [kPa]	σ_{ff} [kPa]	σ_{nn} [kPa]	σ_{ff} [kPa]	σ_{nn} [kPa]	σ_{ff} [kPa]	σ_{nn} [kPa]	σ_{ff} [kPa]	σ_{nn} [kPa]
1.00	0.00	0.00	0.00	0.00	0.00	0.00	0.00	0.00	0.00	0.00
1.01	0.00	0.01	0.00	0.00	0.04	0.04	0.04	0.02	0.16	0.26
1.02	0.01	0.05	0.08	0.01	0.08	0.08	0.07	0.02	0.24	0.34
1.03	0.24	0.07	0.20	0.10	0.16	0.14	0.20	0.09	0.33	0.47
1.04	0.50	0.23	0.38	0.18	0.31	0.23	0.30	0.13	0.47	0.68
1.05	0.85	0.45	0.68	0.36	0.49	0.37	0.55	0.24	0.63	0.81
1.06	1.37	0.78	1.09	0.54	0.76	0.54	0.87	0.38	0.78	1.11
1.07	2.16	1.28	1.66	1.84	1.13	0.85	1.33	0.57	1.06	1.42
1.08	3.40	2.01	2.55	1.27	1.69	1.30	2.06	0.86	1.35	1.80
1.09	5.30	3.13	3.82	1.94	2.51	1.88	3.12	1.20	1.83	2.32
1.10	8.26	4.79	5.87	2.76	3.67	2.80	4.75	1.72	2.44	3.03

2.2 Experimental dataset (Porcine Semilunar Heart Valve Cusps)

To assess the model's generalizability, the framework was further validated using semilunar heart valve cusps—a cardiovascular tissue type structurally distinct from myocardial tissue (Hudson et al., 2022). The validation dataset originated from biaxial mechanical tests performed on approximately $6.5 \times 6.5 \, \text{mm}$ square specimens excised from porcine aortic and pulmonary valve cusps (Hudson et al., 2022). Experimental data were collected under displacement-controlled loading protocols, which applied seven distinct stretch ratios to vary the fiber-to-normal (radial) stretch relationships (Hudson et al., 2022). These ratios included an equibiaxial condition ($1:1$) and six non-equibiaxial loading scenarios ($1:0.25$, $1:0.5$, $1:0.75$, $0.75:1$, $0.5:1$, and $0.25:1$), enabling a comprehensive evaluation of anisotropic tissue behavior under heterogeneous deformation states (Hudson et al., 2022).

Table 2: **Biaxial extension data** recorded during displacement-controlled biaxial extension of porcine semilunar-valve cusp specimens ($\approx 6.5 \times 6.5$ mm^2). Seven proportional loading paths were applied by prescribing paired stretch ratios in the collagen-fiber direction Indices f and n denote the fiber direction and the normal direction, respectively. (Hudson et al., 2022)

λ [-]	$\lambda_f = \lambda$ $\lambda_n = \lambda$		$\lambda_f = \lambda$ $\lambda_n = 0.25\lambda$		$\lambda_f = \lambda$ $\lambda_n = 0.50\lambda$		$\lambda_f = \lambda$ $\lambda_n = 0.75\lambda$		$\lambda_f = 0.25\lambda$ $\lambda_n = \lambda$		$\lambda_f = 0.50\lambda$ $\lambda_n = \lambda$		$\lambda_f = 0.75\lambda$ $\lambda_n = \lambda$	
	σ_{ff} [kPa]	σ_{nn} [kPa]	σ_{ff} [kPa]	σ_{nn} [kPa]	σ_{ff} [kPa]	σ_{nn} [kPa]	σ_{ff} [kPa]	σ_{nn} [kPa]	σ_{ff} [kPa]	σ_{nn} [kPa]	σ_{ff} [kPa]	σ_{nn} [kPa]	σ_{ff} [kPa]	σ_{nn} [kPa]
1.000	0.000	0.000	0.000	0.000	0.000	0.000	0.000	0.000	0.000	0.000	0.000	0.000	0.000	0.000
1.010	0.003	0.007	0.003	0.007	0.004	0.007	0.004	0.006	0.004	0.006	0.004	0.005	0.004	0.004
1.020	0.005	0.013	0.006	0.013	0.007	0.012	0.008	0.012	0.008	0.011	0.008	0.010	0.008	0.007
1.030	0.008	0.021	0.010	0.020	0.012	0.019	0.013	0.018	0.013	0.017	0.014	0.015	0.013	0.010
1.040	0.012	0.031	0.015	0.030	0.018	0.028	0.019	0.027	0.020	0.025	0.021	0.022	0.020	0.015
1.050	0.017	0.045	0.023	0.043	0.026	0.040	0.028	0.038	0.030	0.036	0.031	0.031	0.030	0.022
1.060	0.025	0.065	0.035	0.062	0.040	0.058	0.043	0.055	0.045	0.051	0.047	0.045	0.046	0.032
1.070	0.039	0.103	0.056	0.096	0.065	0.089	0.071	0.083	0.074	0.078	0.078	0.068	0.079	0.049
1.080	0.073	0.216	0.111	0.188	0.132	0.166	0.146	0.152	0.156	0.139	0.169	0.120	0.183	0.085
1.090	0.180	0.651	0.315	0.565	0.404	0.482	0.463	0.423	0.505	0.372	0.562	0.295	0.623	0.178
1.100	0.280	0.960	0.503	0.864	0.655	0.756	0.749	0.662	0.817	0.577	0.896	0.444	0.968	0.250

2.3   Constitutive model

To describe the deformation of a test specimen, we define the mapping

$$\varphi : X \mapsto x = \varphi(X),$$

which carries material points X in the reference configuration to points x in the deformed configuration. The deformation gradient is then

$$F = \nabla_X \varphi,$$

with the requirement that the Jacobian

$$J = \det(F) > 0. \tag{1}$$

By multiplying F on the left or right by its transpose, we obtain the left and right Cauchy–Green tensors,

$$b = F F^{\mathrm{T}} \quad \text{and} \quad C = F^{\mathrm{T}}F,$$

respectively. In the undeformed state, $F = I$, $b = I$, $C = I$, and hence $J = 1$. Values of J below unity $(0 < J < 1)$ indicate volume compression, whereas $J > 1$ signifies volume extension (Holzapfel, 2000; Flaschel et al., 2021).

A transversely isotropic material is specified by a single preferred direction given by the unit vector n^0 (with $\|n^0\| = 1$) in the reference configuration, which deforms into $n = F \cdot n^0$ in the current configuration, and by the corresponding structure tensor $N = n^0 \otimes n^0$. Under these assumptions, the deformation of our transversely isotropic tissue samples can be fully described by the two isotropic invariants

$$I_1 = [F^{\mathrm{T}}F] : I \quad I_2 = \left[I_1^2 - (F^{\mathrm{T}}F) : (F^{\mathrm{T}}F) \right] \quad I_3 = \det\left(F^T F\right) = J^2 \tag{2}$$

together with the four anisotropic invariants associated with the stretches squared in fiber and normal axis:

$$I_{4,f} = [F^{\mathrm{T}}F] : [n_1^0 \otimes n_1^0] \quad I_{4,n} = [F^{\mathrm{T}}F] : [n_2^0 \otimes n_2^0]$$
$$I_{5,f} = [F^{\mathrm{T}}F]^2 : [n_1^0 \otimes n_1^0] \quad I_{5,n} = [F^{\mathrm{T}}F]^2 : [n_2^0 \otimes n_2^0] \tag{3}$$
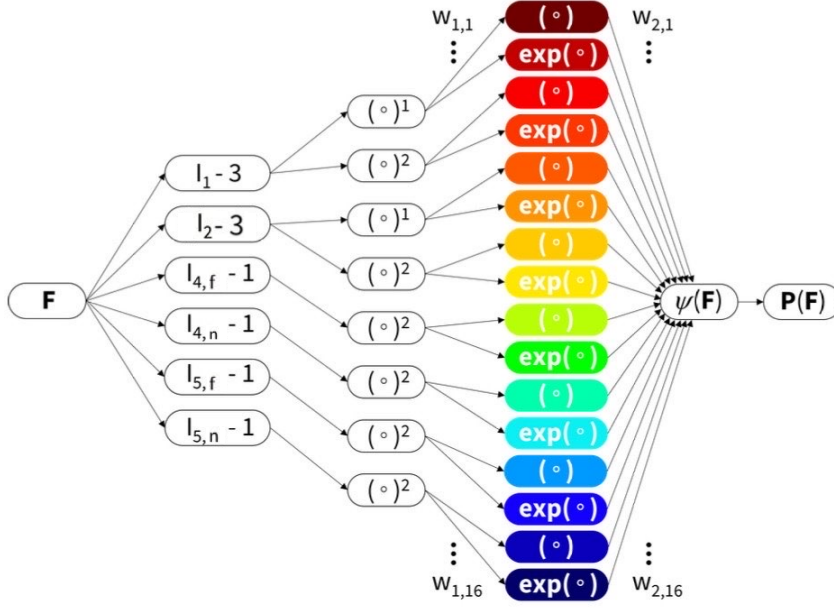
Figure 1: **Constitutive neural network** Transversely isotropic, perfectly incompressible, constitutive neural network with two hidden layers to approximate the free-energy function $\psi\big(I_1, I_2, I_{4,f}, I_{4,n}, I_{5,f}, I_{5,n}\big)$. The first layer generates powers $(\circ)$ and $(\circ)^2$ of the zeroth input, and the second layer applies the identity $(\circ)$ and the exponential function $\exp(\circ)$ to these powers. Adapted from *Atrial constitutive neural networks* (Figure 1), by M. Peirlinck, K. Linka, & E. Kuhl, 2025, arXiv preprint `arXiv:2504.02748` [cs.CE], p. 4. Copyright 2025 by the authors.

where n_1^0 and n_2^0 denote the unit vectors along the two internal fiber directions in the undeformed (reference) configuration (Peirlinck et al., 2024c).

For a perfectly incompressible material one enforces $J = \det F = I_3 = 1$, which removes any volumetric degree of freedom and leaves only the six invariants I_1, I_2, $I_{4,f}$, $I_{4,n}$, $I_{5,f}$, $I_{5,n}$ as independent descriptors of the deformation.

We next define the constitutive equation as the tensor-valued mapping between the deformation gradient F and the Piola (nominal) stress P. In particular,

$$P = P(F), \qquad P = \lim_{dA \to 0} \frac{df}{dA}, \tag{4}$$

where df is the force acting on an infinitesimal undeformed area dA. Rather than learning this full tensor-to-tensor relation $P(F)$ with a conventional neural network, our goal is to build a Constitutive Artificial Neural Network whose architecture a priori restricts the space of admissible functions so that key thermodynamic and physical principles are automatically satisfied.

We began by digitizing the published Green–Lagrange strain vs. second Piola–Kirchhoff stress curves and then applied the standard pull-back relations to recover the in-plane principal stretches λ_1, λ_2 together with their corresponding nominal Piola stress components $\hat{P}_1, \hat{P}_2$. In the special case of homogeneous biaxial extension we impose two principal stretches $\lambda_1 \geq 1$, $\lambda_2 \geq 1$ along orthogonal directions and enforce incompressibility through $\det F = \lambda_1 \lambda_2 \lambda_3 = 1$, which yields the thickness stretch $\lambda_3 = (\lambda_1 \lambda_2)^{-1} \leq 1$. Guided by polarized-light microscopy of atrial tissue, we assume two orthogonal fiber families that remain orthonormal and shear-free during loading. Hence the deformation gradient takes the diagonal form,

$$F = \text{diag}\{\lambda_1, \lambda_2, (\lambda_1 \lambda_2)^{-1}\}. \tag{5}$$

For isotropic invariants,

$$I_1 = \lambda_1^2 + \lambda_2^2 + (\lambda_1 \lambda_2)^{-2}, \quad I_2 = \lambda_1^{-2} + \lambda_2^{-2} + (\lambda_1 \lambda_2)^2 \tag{6}$$

And for anisotropic invariants,

$$I_{4,f} = \lambda_1^2, I_{4,n} = \lambda_2^2, I_{5,f} = \lambda_1^4, I_{5,n} = \lambda_2^4. \tag{7}$$

To enforce thermodynamic consistency, we introduce the Helmholtz free-energy as a function of the deformation gradient, $\psi = \psi(F)$. Assuming purely elastic behavior (no internal dissipation) and by reformulating the Clausius–Duhem entropy inequality according to the Coleman–Noll approach (Coleman and Noll, 1959), one finds that the first Piola–Kirchhoff stress must satisfy $P = \frac{\partial \psi}{\partial F}$. Writing the free-energy in terms of the six invariants I_1, I_2, $I_{4,f}$, $I_{4,n}$, $I_{5,f}$, $I_{5,n}$ gives the compact relation

$$P = \frac{\partial \, \psi\bigl(I_1, I_2, I_{4,f}, I_{4,n}, I_{5,f}, I_{5,n}\bigr)}{\partial F}. \tag{8}$$

We enforce polyconvexity by avoiding arbitrary products of convex functions—which generally are not convex—and instead adopting, as in, a free-energy ansatz built as a sum of individually polyconvex polynomial subfunctions (Hartmann and Neff, 2003). Concretely, we write

$$\psi(F) = \psi_1(I_1) + \psi_2(I_2) + \psi_4(I_{4,f}) + \psi_4(I_{5,n}) + \psi_5(I_{5,f}) + \psi_5(I_{5,n}), \tag{9}$$

so that each $\psi_1, \psi_2, \psi_{4,ii}, \psi_{5,ii}$ is convex in its scalar argument. From this decomposition the first Piola–Kirchhoff stress follows by chain-rule differentiation:

$$P = \frac{\partial \psi}{\partial I_1}\frac{\partial I_1}{\partial F} + \frac{\partial \psi}{\partial I_2}\frac{\partial I_2}{\partial F} + \frac{\partial \psi}{\partial I_{4,f}}\frac{\partial I_{4,f}}{\partial F} + \frac{\partial \psi}{\partial I_{4,n}}\frac{\partial I_{4,n}}{\partial F} + \frac{\partial \psi}{\partial I_{5,f}}\frac{\partial I_{5,f}}{\partial F} + \frac{\partial \psi}{\partial I_{5,n}}\frac{\partial I_{5,n}}{\partial F}. \tag{10}$$

Under the assumptions of homogeneous, shear-free biaxial extension and a traction-free condition normal to the tissue plane, (Peirlinck et al., 2024b) one can show analytically that the in-plane first Piola–Kirchhoff stresses P_1 and P_2 depend on the principal stretches λ_1, λ_2 as follows:

$$
\begin{aligned}
P_1 &= 2\left[\lambda_1 - (\lambda_1^2\lambda_2^2)^{-1}\right]\frac{\partial \psi}{\partial I_1} + 2\left[\lambda_1\lambda_2^2 - \lambda_1^{-3}\right]\frac{\partial \psi}{\partial I_2} + 2\lambda_1\frac{\partial \psi}{\partial I_{4,f}} + 4\lambda_1^3\frac{\partial \psi}{\partial I_{5,f}}, \\
P_2 &= 2\left[\lambda_2 - (\lambda_1^2\lambda_2^2)^{-1}\right]\frac{\partial \psi}{\partial I_1} + 2\left[\lambda_1^2\lambda_2 - \lambda_2^{-3}\right]\frac{\partial \psi}{\partial I_2} + 2\lambda_2\frac{\partial \psi}{\partial I_{4,n}} + 4\lambda_2^3\frac{\partial \psi}{\partial I_{5,n}}.
\end{aligned} \tag{11}
$$

2.4 Constitutive neural network

To determine the optimal constitutive description and parameter set for the atrial tissue's biaxial response, we employ a constitutive neural network—an architecture that by design enforces thermodynamic consistency, material objectivity and symmetry, perfect incompressibility, polyconvexity, and other physical constraints (Linka and Kuhl, 2023). As shown in Figure1, our network, informed by atrial microstructure, assumes transverse isotropy and incompressibility and has two hidden layers with 6, 8, and 16 neurons, respectively. The zeroth layer computes six normalized invariants from the deformation gradient
F:$[I_1 - 3]$, $[I_2 - 3]$, $[I_{4,f} - 1]$, $[I_{4,n} - 1]$, $[I_{5,f} - 1]$, $[I_{5,n} - 1]$,
ensuring $\psi = 0$ when $F = I$. The first hidden layer then generates each invariant's first and second powers, $\circ$ and $\circ^2$, and the second hidden layer applies two smooth, monotonic, continuously differentiable, unbounded activations—namely the identity, $\circ$, and the exponential, $\exp(\circ)$—to those powers, thereby satisfying all standard constitutive requirements and polyconvexity by construction (Linka and Kuhl, 2023; Linden et al., 2023; Hartmann and Neff, 2003).

The resulting total free-energy function takes the explicit form

$$
\begin{aligned}
\psi = &\; w_{2,1}w_{1,1}\,[I_1 - 3] + w_{2,2}\left[\exp\bigl(w_{1,2}[I_1 - 3]\bigr) - 1\right] + w_{2,3}w_{1,3}\,[I_1 - 3]^2 + w_{2,4}\left[\exp\bigl(w_{1,4}[I_1 - 3]^2\bigr) - 1\right] \\
&+ w_{2,5}w_{1,5}\,[I_2 - 3] + w_{2,6}\left[\exp\bigl(w_{1,6}[I_2 - 3]\bigr) - 1\right] + w_{2,7}w_{1,7}\,[I_2 - 3]^2 + w_{2,8}\left[\exp\bigl(w_{1,8}[I_2 - 3]^2\bigr) - 1\right] \\
&+ w_{2,9}w_{1,9}\,[I_{4,f} - 1]^2 + w_{2,10}\left[\exp\bigl(w_{1,10}[I_{4,f} - 1]^2\bigr) - 1\right] + w_{2,11}w_{1,11}\,[I_{4,n} - 1]^2 + w_{2,12}\left[\exp\bigl(w_{1,12}[I_{4,n} - 1]^2\bigr) - 1\right]
\end{aligned}
$$

$$+ w_{2,13} w_{1,13} [I_{5,f} - 1]^2 + w_{2,14} [\exp(w_{1,14}[I_{5,f} - 1]^2) - 1] + w_{2,15} w_{1,15} [I_{5,n} - 1]^2 + w_{2,16} [\exp(w_{1,16}[I_{5,n} - 1]^2) - 1]. \quad (12)$$

We leverage TensorFlow's automatic differentiation to obtain the six free-energy gradients

$$\frac{\partial \psi}{\partial I_1}, \frac{\partial \psi}{\partial I_2}, \frac{\partial \psi}{\partial I_{4,f}}, \frac{\partial \psi}{\partial I_{4,n}}, \frac{\partial \psi}{\partial I_{5,f}}, \frac{\partial \psi}{\partial I_{5,n}}, \quad (13)$$

which enter directly into the Piola stress expressions in Eq.(10). Our network contains 2×16 scalar weights $\mathbf{w}$, each constrained to satisfy $w_i \geq 0$. These weights are fitted by minimizing a loss function L that combines the mean squared error between the model predictions $P_1(\lambda_{1,j}, \lambda_{2,j})$, $P_2(\lambda_{1,j}, \lambda_{2,j})$ and the experimental stresses $\hat{P}_{1,j}, \hat{P}_{2,j}$ over n_{trn} training points, with an ℓ_p-norm regularizer weighted by a nonnegative coefficient α:

$$L = \frac{1}{n_{\text{trn}}} \sum_{j=1}^{n_{\text{trn}}} \left\| P_1(\lambda_{1,j}, \lambda_{2,j}) - \hat{P}_{1,j} \right\|^2 + \frac{1}{n_{\text{trn}}} \sum_{j=1}^{n_{\text{trn}}} \left\| P_2(\lambda_{1,j}, \lambda_{2,j}) - \hat{P}_{2,j} \right\|^2 + \alpha \left\| \mathbf{w} \right\|_p^p \longrightarrow \min, \quad (14)$$

where $\|\mathbf{w}\|_p^p = \sum_{i=1}^{n_{\text{par}}} |w_i|^p$ and $\alpha \geq 0$. Training is carried out using the ADAM optimizer (Kingma and Ba, 2014).

3 Results

The Constitutive Artificial Neural Network shown in Fig 1 was successfully trained with the biaxial extension data for human myocardium provided in Table 1 (Sommer et al., 2015). In every case, the loss function converged reliably within 30,000 epochs, aided by an early-stopping rule that terminated training when the accuracy plateaued. Using a batch size of 32, each run on Google Colab took about 20–30 minutes; the exact duration depended on the amount of training data and the level of regularization. For every dataset and loading direction, we compared the experimentally reported stress–shear and stress–stretch responses with those predicted by the learned stress–stretch model. Model performance was assessed with the correlation coefficient (R^2) and the root-mean-square error (rms) for both training and testing. We also report the mean values of these two metrics across all testing modes, covering the five biaxial-extension ratios applied in each of the two principal directions.
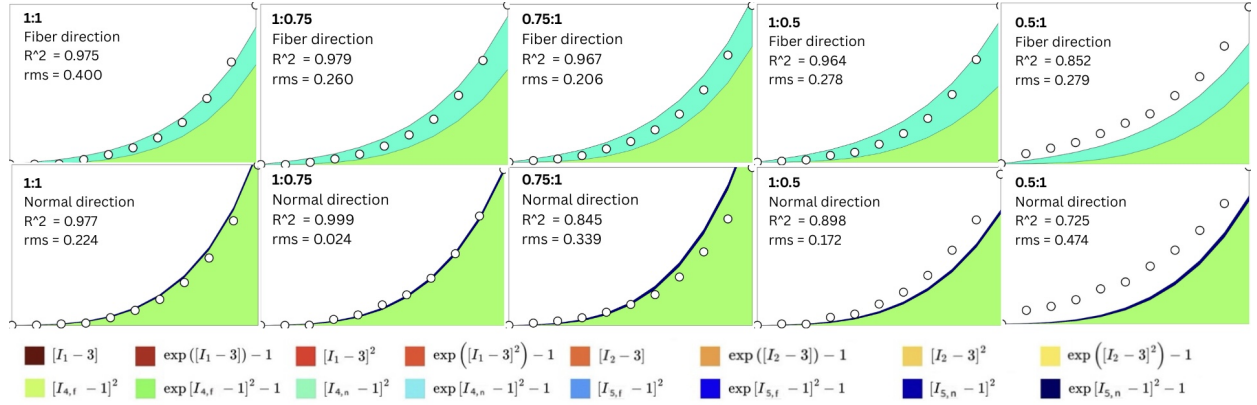

Figure 2: **Discovered constitutive model for human myocardial tissue.** Each scratched ratio, direction, and individual stretch–stress curve's R^2 goodness of fit with respect to the original experimental data is shown in the top-left corner. Color map adapted from *Atrial constitutive neural networks* (Figure 2), by M. Peirlinck, K. Linka, & E. Kuhl, 2025, arXiv preprint `arXiv:2504.02748` [cs.CE], p. 6. Copyright 2025 by the authors.

Using L_1 regularization with the penalty weight varied over $\alpha \in \{10.0, 1.0, 0.1, 0.01\}$, we find that $\alpha = 0.01$ achieves the best trade-off between parameter sparsity and fit quality.

Fig 2 summarizes the quantitative fidelity of our Constitutive ANN in reproducing the biaxial stress–strain response along both the fibre and normal axes at five prescribed loading ratios (fibre:normal=1:1, 1:0.75, 0.75:1, 1:0.5 and 0.5:1). Each panel reports the coefficient of determination (R²) and root-mean-square error (rms) between the network's predictions (shaded region) and the training data (white markers). Taken across all five protocols, the model attains an average R² of 0.614 and an average rms of 0.261 in the fibre direction, and an average R² of 0.888 with an average rms of 0.243 in the normal direction, indicating generally good agreement but revealing systematic variation with loading path.

3.1 Performance in the fibre direction

Fiber-direction performance is consistently strong, with an average $R^2 = 0.947$ and rms $= 0.285$. The best fit in the fiber axis occurs at the $1 : 0.75$ ratio ($R^2 = 0.979$, rms $= 0.260$), closely followed by the equibiaxial $1 : 1$ loading ($R^2 = 0.975$, rms $= 0.400$). Even under pronounced fiber compression ($0.5 : 1$), the network maintains reasonable accuracy ($R^2 = 0.852$, rms $= 0.279$), although this represents the lowest fidelity in the fiber direction. Mid-range conditions such as $0.75 : 1$ ($R^2 = 0.967$, rms $= 0.206$) and $1 : 0.5$ ($R^2 = 0.964$, rms $= 0.278$) also exhibit very good fits, indicating the model captures both the stiffening under fiber stretch and the softening under fiber compliance.

3.2 Performance in the normal direction

Normal-direction performance shows greater variability with loading ratio, yielding an average $R^2 = 0.889$ and rms $= 0.247$. Peak accuracy is attained at the $1 : 0.75$ ratio ($R^2 = 0.999$, rms $= 0.024$)—an almost perfect fit—followed by equibiaxial loading ($R^2 = 0.977$, rms $= 0.224$) and the $1 : 0.5$ case ($R^2 = 0.898$, rms $= 0.172$). However, when the fiber stretch is reduced below unity (e.g., $0.75 : 1$), the normal-axis fit degrades ($R^2 = 0.845$, rms $= 0.339$), and it deteriorates further at the lowest fiber stretch of $0.5 : 1$ ($R^2 = 0.725$, rms $= 0.474$). These trends suggest that while the model captures normal-direction responses well under fiber-dominant loading, it struggles to reproduce the mechanical behavior when fibers are under compression and the normal axis carries the majority of the load.

3.3 Discovered Free-Energy Function

The network discovers free-energy functions with three terms of anisotropic invariants: one term is , $\exp\left([I_{4,f} - 1]^2\right) - 1$ shown in the lime green colors. There are $\left[I_{4,f} - 1\right]^2$ terms shown in the turquoise colors and the other is a function of another of the invariants $\exp\left([I_{5,n} - 1]^2\right) - 1$, shown in the deep navy blue colors. The discovered model contains three parameters,

Interestingly, we discover an three-terms model that exclusively automated model discovery for human myocardial tissue (Sommer et al., 2015),

$$
\begin{aligned}
\Psi = {} & w_{2,10}\left[\exp\left(w_{1,10}(I_{4,f} - 1)^2\right) - 1\right] \\
& + w_{1,11}\, w_{2,11}\, (I_{4,n} - 1)^2 \\
& + w_{2,16}\left[\exp\left(w_{1,16}(I_{5,n} - 1)^2\right) - 1\right].
\end{aligned}
$$

Define
$$
a_1 = w_{2,10},\ b_1 = w_{1,10}; \quad a_2 = w_{2,12},\ b_2 = w_{1,12}; \quad a_3 = w_{2,16},\ b_3 = w_{1,16}.
$$

$$
\begin{aligned}
\Psi = {} & a_1\left[\exp\left(b_1\,(I_{4,f} - 1)^2\right) - 1\right] \\
& + a_2\,(I_{4,n} - 1)^2 \\
& + a_3\left[\exp\left(b_3\,(I_{5,n} - 1)^2\right) - 1\right].
\end{aligned}
$$

Here,

$$
a_1 = 2.3851, \quad b_1 = 14.8176, \quad a_2 = 10.8410 * 0.10993 = 1.1911, \quad a_3 = 1.3237, \quad b_3 = 0.082274.
$$

So the model reads;
$$
\begin{aligned}
\Psi = {} & 2.3851\left[\exp\left(14.8176\,(I_{4,f} - 1)^2\right) - 1\right] \\
& + 1.1911\,(I_{4,n} - 1)^2 \\
& + 1.3237\left[\exp\left(0.082274\,(I_{5,n} - 1)^2\right) - 1\right].
\end{aligned}
$$

Remarkably, out of the $2^{16} = 65,536$ candidate models, the optimal three-term network retains only (i) the squared fourth-invariant contribution, (ii) its exponential map, and (iii) the exponential of the squared fifth invariant to capture the tissue's anisotropic response. Furthermore, the fourth invariant alone predominates in describing the anisotropic behavior of human myocardium (Sommer et al., 2015). There are no isotropic terms included here.
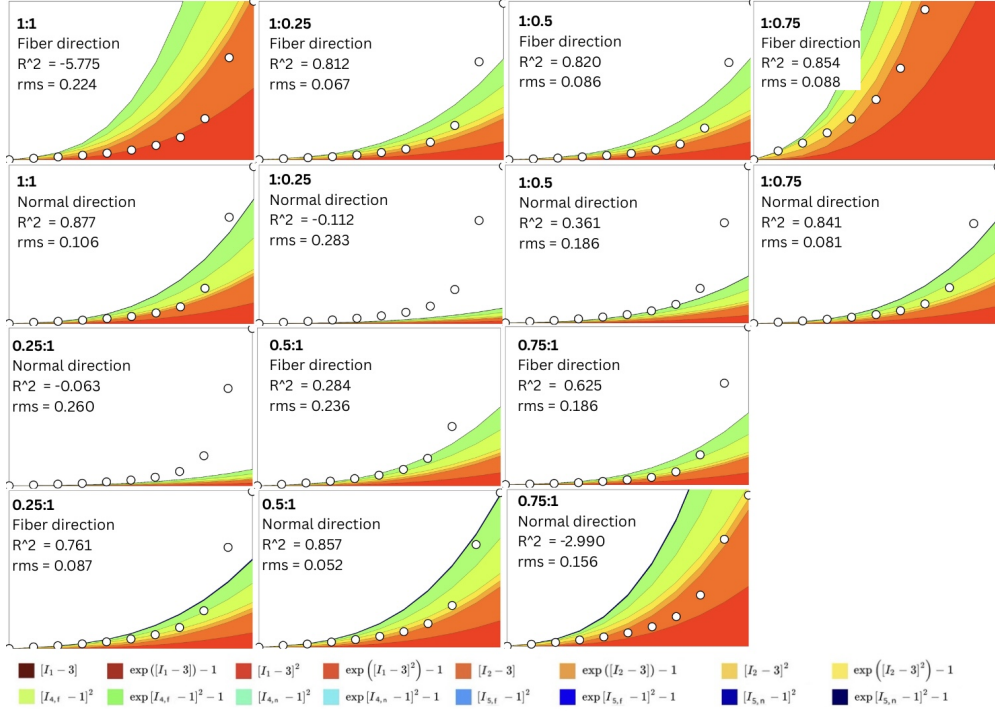
Figure 3: **Discovered constitutive model for porcine semilunar valve cusp.** Each scratched ratio, direction, and individual stretch–stress curve's R^2 goodness of fit with respect to the original experimental data is shown in the top-left corner. Each term colour map adapted from *Atrial constitutive neural networks* (Figure 2), by M. Peirlinck, K. Linka, & E. Kuhl, 2025, arXiv preprint `arXiv:2504.02748` [cs.CE], p. 4. Copyright 2025 by the authors.

3.4   Performance Evaluation on Porcine Semilunar Valve Cusp Data

Figure 3 shows the performance of our myocardial-trained CANN when applied "as-is" to porcine semilunar valve cusp data (Sommer et al., 2015; Hudson et al., 2022). Across the seven biaxial loading conditions tested on porcine semilunar valve cusps, our myocardial-trained CANN yields a mean $R^2 = -0.132$ and an overall RMS error of 0.150, indicating that, on average, its predictions are worse than a constant-mean baseline (Sommer et al., 2015). Notably, the network performs reasonably well under moderate, fiber-dominated stretches—fiber directions at $1:0.25\,(R^2 = 0.812$, rms $= 0.067)$, $1:0.5\,(R^2 = 0.820$, rms $= 0.086)$, and $1:0.75\,(R^2 = 0.854$, rms $= 0.088)$—and in the normal direction at equibiaxial ($1:1$, $R^2 = 0.877$, rms $= 0.106$), $1:0.75$ ($R^2 = 0.841$, rms $= 0.081$), and $0.5:1$ ($R^2 = 0.857$, rms $= 0.052$) loading, where R^2 values exceed 0.80 and RMS errors remain below 0.11. In stark contrast, predictions collapse under extreme or off-axis loading: the equibiaxial fiber case ($1:1$) yields $R^2 = -5.775$ (rms $= 0.224$), the off-axis normal case at $0.75:1$ gives $R^2 = -2.990$ (rms $= 0.156$), and low-fiber, high-normal regimes (normal at $1:0.25$ and $0.25:1$) produce negative R^2 values with large RMS errors (> 0.26). Even fiber compression at $0.5:1$ delivers only modest agreement ($R^2 = 0.284$, rms $= 0.236$) (Hudson et al., 2022).

This pronounced failure underscores two intertwined issues: model misspecification and overfitting to myocardial-specific features (Sommer et al., 2015; Chicco et al., 2021; Alexander et al., 2015). Semilunar valve cusps differ markedly from myocardium in collagen fiber orientation, cross-link density, and extracellular matrix composition, giving rise to distinct anisotropic and bending responses that our myocardial-centric network cannot capture (Sommer et al., 2015). Although L1 regularization induced sparsity, it likely pruned parameters critical for modeling low-stress, transverse cusp behavior, leaving the network ill-equipped to interpolate or extrapolate beyond its training domain. Moreover, subtle noise patterns ingrained during training on myocardial data further degrade cusp predictions, as the model effectively fits tissue-specific idiosyncrasies rather than learning universal constitutive laws (Sommer et al., 2015).

4 Discussion

The aim of this work was to identify the model form and associated parameters that most accurately capture the mechanical behavior of human myocardial tissue (Sommer et al., 2015). To this end, we implemented constitutive neural networks augmented with L1-regularization. We systematically examine and discuss the primary characteristics and difficulties associated with model discovery. Our analysis uncovers several noteworthy trends that traditional parameter-identification techniques alone would be incapable of revealing.

Our constitutive neural network uncovers sparse, interpretable representations of human myocardial tissue mechanics. As shown in Figure 1, the network comprises sixteen individual terms—two isotropic components and four anisotropic components corresponding to the two axes of the biaxial loading data—yielding 2^{16}, or over sixty-five thousand, possible term combinations encoded through the network's weights (Sommer et al., 2015). We begin by training the network on biaxial extension data under a range of L1-regularization strengths, and we find that it converges reliably on the human myocardial tissue datasets, successfully identifying models that reproduce the observed training behavior (Sommer et al., 2015; Peirlinck et al., 2024b,a).

We consistently observe identical anisotropic constitutive contributions along both the fiber and normal axes, manifested by an exponential quadratic fourth invariant term in the fiber direction, specifically $\exp\left([I_{4,f} - 1]^2\right) - 1$. The models we uncover further emphasize the necessity of a fifth-invariant $I_{4,n}$ component to capture the nonlinear quadratic stiffness unique to the fiber axis, while a sixth-invariant $I_{5,n}$ term is required to describe the nonlinear exponential-quadratic stiffness confined to the normal axis. Together, these insights yield compact, three-term constitutive formulations that provide exceptionally accurate representations of the passive mechanical behavior of human myocardial tissue (Sommer et al., 2015).

This performance gap form human myocardial tissue model on porcine semilunar valve cusps data underscores a fundamental domain shift: although porcine semilunar cusps share some mechanical traits with myocardium, their constitutive responses under anisotropic and bending loads differ sufficiently that a model trained exclusively on human myocardial tissue cannot reliably interpolate or extrapolate to cusp behavior (Sommer et al., 2015; Hudson et al., 2022). To achieve accurate cusp predictions, we must reconfigure the network—either by augmenting its training set with porcine cusp data or by adapting its architecture to explicitly capture valve-specific anisotropy and bending stiffness. Future work will focus on integrating cusp-derived mechanical measurements and exploring multi-tissue training regimes to build a more universally applicable cardiac tissue constitutive model.

Recognizing the inherent variability among biological specimens, subsequent investigations should validate these identified constitutive models by performing biaxial tensile tests on additional samples harvested from the same anatomical regions of human myocardium (Sommer et al., 2015; Peirlinck et al., 2019, 2020). To achieve this, we propose a hierarchical, data-driven framework that aggregates biaxial loading data across multiple specimens and patients to derive a single, best-fit constitutive formulation—mirroring recent methodologies applied to pulmonary arterial tissue. Within this scheme, we will carefully balance the trade-off between individual specimen R^2 goodness-of-fit values and a global R^2 metric that reflects model performance across the entire pooled dataset. (Linka et al., 2024; Peirlinck et al., 2020).

For decades, the prevailing paradigm in constitutive modeling has been to choose a candidate model a priori and subsequently fit its parameters to experimental data (Avril et al., 2010; Fehervaryn et al., 2016; Linden et al., 2022). Efforts to enhance model accuracy have typically involved incremental adjustments to existing terms or the gradual substitution of individual components. This incremental approach was necessitated by the formidable nonlinearity, non-convexity, and profusion of local minima inherent to the parameter-identification problem, as well as the substantial computational demands of exploring the model space. Today, however, the convergence of vastly increased computational capacity and highly efficient numerical solvers creates a singular opportunity to concurrently identify both the optimal constitutive form and its corresponding parameters directly from experimental observations.

5 Conclusion

Unlike traditional approaches that perform well under isolated loading modes—tension, compression, or shear—but struggle when calibrated across multiple tests, we employ incompressible, transversely isotropic constitutive neural networks to discover both the optimal model form and its parameters concurrently. By training on five biaxial extension experiments and enforcing sparsity through L1-regularization, our findings indicate that an accurate constitutive description of cardiac tissue requires at least three anisotropic invariants. The resulting minimal three-term formulation retains only (i) the squared fourth invariant, (ii) its exponential mapping, and (iii) the exponential of the squared fifth invariant to capture the myocardium's anisotropic mechanics; importantly, the fourth invariant alone predominates in characterizing the tissue's directional response, and no isotropic contributions are included.

Our findings demonstrate that constitutive neural networks are capable of identifying both the underlying constitutive form and its parameters to reliably reproduce the deformation and stress behavior of human myocardial tissue under physiologically realistic loading conditions. We foresee that this concise, three-term formulation will drive progress in the design of cardiovascular implants and devices, improve the precision of diagnostic tools, and inform more effective approaches to the treatment and management of heart disease.

Declaration of AI-Tool Usage and Model Attribution

I hereby declare that I have used ChatGPT to assist in the preparation of this journal. Specifically, ChatGPT supported the refinement of language, grammar, and overall writing style.

I also acknowledge that the computational model developed in this project is based on previously published Constitutive Artificial Neural Network (CANN) frameworks. The original models were obtained from openly available resources and publications, which served as foundational work for my adaptations. The key references are as follows:

1. Wang, Z., et al. (2022). *A new family of Constitutive Artificial Neural Networks towards automated model discovery*. Computer Methods in Applied Mechanics and Engineering, 398, 115731. `https://doi.org/10.1016/j.cma.2022.115731`

2. Liu, J., et al. (2023). *Automated model discovery for skin: Discovering the best model, data, and experiment*. Computer Methods in Applied Mechanics and Engineering, 410, 116007. `https://doi.org/10.1016/j.cma.2023.116007`

3. Liu, J., et al. (2024). *Automated model discovery for human cardiac tissue: Discovering the best model and parameters*. Computer Methods in Applied Mechanics and Engineering, 424, 117078. `https://doi.org/10.1016/j.cma.2024.117078`

These works informed the theoretical foundation, architecture, and modeling approach used in this thesis. Modifications to the models for the application to human myocardial tissue were carried out independently by the author.

6   Appendices

6.1   Model Availability

The complete source code, data, and notebooks for this project are available at
https://github.com/NickyGitHub1/CANNs_2937475M.

6.2   Interim Report

The full interim report is available at: `https://gla-my.sharepoint.com/:b:/g/personal/2937475m_student_gla_ac_uk/EaZLOzBDD_JCmy03qGIPeBUBtd5JMwqLc7JLqzR8zr4c9g`

Note: The interim report describes a preliminary model structure. The final, revised model—different in architecture and performance—is detailed in this document.

6.3   Project Timeline

- **October 2024**

    - **Objectives:** Review available materials; determine the most suitable modelling approach; clarify model requirements.

    - **Activities:** Met with Dr. Ankush Aggarwal to review notes and datasets; discussed AI modelling options; agreed to proceed with CANNs.

    - **Deliverable:** Confirmation to proceed with CANNs; agreed list of datasets, key papers, and next steps.

    - **Resources:** Dr. Aggarwal's expertise and meeting notes; existing datasets and literature; meeting facilities.

- **November 2024**

    - **Objectives:** Prepare and submit the preliminary report for review.

    - **Activities:** Drafted the preliminary report; emailed it to Dr. Aggarwal for feedback and submission.

    - **Deliverable:** Preliminary report submitted to supervisor; awaiting review comments.

    - **Resources:** Preliminary report document.

- **December 2024**

    - **Objectives:** Understand and reproduce the reference model; verify reproducibility; deepen knowledge via literature review.

    - **Activities:** Obtained original model code/data; ran the model to match published outputs; compared results; summarized key papers.

    - **Deliverable:** Replication report with comparison results; annotated bibliography.

    - **Resources:** Reference model code and dataset; published papers; supervisor feedback sessions.

- **January 2025**

    - **Objectives:** Outline model improvements; reflect on shortcomings; plan next steps.

    - **Activities:** Wrote interim report; noted over-reliance on reference implementation and underperformance; highlighted differences; submitted to Dr. Aggarwal.

    - **Deliverable:** Interim report with critique and revised plan.

    - **Resources:** Interim report document; preliminary model code and results; supervisor feedback.

- **February 2025**

  - **Objectives:** Adapt model structure; address performance issues; clarify material properties.
  - **Activities:** Continued development; identified over-reliance and under-fitting; met with Dr. Aggarwal to refine architecture and discuss dataset properties.
  - **Deliverable:** Action plan for revised architecture; summary of dataset properties and targets.
  - **Resources:** Supervisor meeting notes; dataset metadata; computing resources.

- **March 2025**

  - **Objectives:** Evaluate and select the optimal model; optimize performance; prepare presentation.
  - **Activities:** Fitted two model variants and compared metrics; met with Dr. Aggarwal to finalize choice; refined the chosen model; delivered slides to faculty.
  - **Deliverable:** Final model decision; performance summary; presentation slides and feedback.
  - **Resources:** Model variants and metrics; supervisor guidance; presentation facilities.

- **April 2025**

  - **Objectives:** Finalize the selected model; complete and submit the final report.
  - **Activities:** Refined and validated the model on the full dataset; consulted with Dr. Aggarwal on structure and conclusions; drafted, polished, and submitted the report on time.
  - **Deliverable:** Final report with finalized model and performance evaluation.
  - **Resources:** Final dataset and codebase; LaTeX/Overleaf; supervisor feedback; computing resources.

References

Alber, M., Tepole, A. B., Cannon, W. R., De, S., Dura-Bernal, S., Garikipati, K., Karniadakis, G., Lytton, W. W., Perdikaris, P., Petzold, L., and Kuhl, E. (2019). Integrating machine learning and multiscale modeling—perspectives, challenges, and opportunities in the biological, biomedical, and behavioral sciences. *NPJ Digital Medicine*.

Alexander, D. L. J., Tropsha, A., and Winkler, D. A. (2015). Beware of r^2: Simple, unambiguous assessment of the prediction accuracy of qsar and qspr models. *Journal of Chemical Information and Modeling*.

Avril, S., Badel, P., and Duprey, A. (2010). Anisotropic and hyperelastic identification of in vitro human arteries from full-field optical measurements. *Journal of Biomechanics*.

Babaei, H., Mendiola, E. A., Neelakantan, S., Xiang, Q., Vang, A., Dixon, R. A. F., Shah, D. J., Vanderslice, P., Choudhary, G., and Avazmohammadi, R. (2022). A machine learning model to estimate myocardial stiffness from edpvr. *Scientific Reports*.

Brunton, S. L., Proctor, J. L., and Kutz, J. N. (2016). Discovering governing equations from data by sparse identification of nonlinear dynamical systems. *Proceedings of the National Academy of Sciences of the United States of America*.

Chicco, D., Warrens, M. J., and Jurman, G. (2021). The coefficient of determination r-squared is more informative than smape, mae, mape, mse and rmse in regression analysis evaluation. *PeerJ Computer Science*.

Coleman, B. D. and Noll, W. (1959). On the thermostatics of continuous media. *Archive for Rational Mechanics and Analysis*.

Fan, R. and Sacks, M. S. (2014). Simulation of planar soft tissues using a structural constitutive model: Finite element implementation and validation. *Journal of Biomechanics*.

Fehervaryn, H., Smoljkić, M., Sloten, J. V., and Famaey, N. (2016). Planar biaxial testing of soft biological tissue using rakes: A critical analysis of protocol and fitting process. *Journal of the Mechanical Behavior of Biomedical Materials*.

Flaschel, M., Kumar, S., and Lorenzis, L. D. (2021). Unsupervised discovery of interpretable hyperelastic constitutive laws. *Computer Methods in Applied Mechanics and Engineering*.

Frank, I. E. and Friedman, J. H. (1993). A statistical view of some chemometrics regression tools. *Technometrics*.

Hadjicharalambous, M., Chabiniok, R., Asner, L., Sammut, E., Wong, J., Carr-White, G., Lee, J., Razavi, R., Smith, N., and Nordsletten, D. (2014). Analysis of passive cardiac constitutive laws for parameter estimation using 3d tagged mri. *Biomech Model Mechanobiol*.

Hartmann, S. and Neff, P. (2003). Polyconvexity of generalized polynomial-type hyperelastic strain energy functions for near-incompressibility. *International Journal of Solids and Structures*.

Holthusen, H., Lamm, L., Brepols, T., Reese, S., and Kuhl, E. (2023). Theory and implementation of inelastic constitutive artificial neural networks. *arXiv preprint arXiv:2311.06380*.

Holzapfel, G. A. (2000). *Nonlinear Solid Mechanics: A Continuum Approach to Engineering*. John Wiley & Sons.

Hudson, L. T., Laurence, D. W., Lau, H. M., Mullins, B. T., Doan, D. D., and Lee, C.-H. (2022). Linking collagen fiber architecture to tissue-level biaxial mechanical behaviors of porcine semilunar heart valve cusps. *Journal of the Mechanical Behavior of Biomedical Materials*.

Kingma, D. P. and Ba, J. (2014). Adam: A method for stochastic optimization. *arXiv preprint arXiv:1412.6980*.

Linden, K. V., Fehervary, H., Maes, L., and Famaey, N. (2022). An improved parameter fitting approach of a planar biaxial test including the experimental prestretch. *Journal of the Mechanical Behavior of Biomedical Materials*.

Linden, L., Klein, D. K., Kalina, K. A., Brummund, J., Weeger, O., and Kästner, M. (2023). Neural networks meet hyperelasticity: A guide to enforcing physics. *Journal of the Mechanics and Physics of Solids*.

Linka, K., Hillgärtner, M., Abdolazizi, K. P., Aydin, R. C., Itskov, M., and Cyron, C. J. (2021). Constitutive artificial neural networks: A fast and general approach to predictive data-driven constitutive modeling by deep learning. *Journal of Computational Physics*.

Linka, K., Holzapfel, G. A., and Kuhl, E. (2024). Discovering uncertainty: Bayesian constitutive artificial neural networks. *bioRxiv*.

Linka, K. and Kuhl, E. (2023). A new family of constitutive artificial neural networks towards automated model discovery. *Computer Methods in Applied Mechanics and Engineering*.

Linka, K., Tepole, A. B., Holzapfel, G. A., and Kuhl, E. (2023). Automated model discovery for skin: Discovering the best model, data, and experiment. *Computer Methods in Applied Mechanics and Engineering*.

Martonová, D., Peirlinck, M., Linka, K., Holzapfel, G. A., Leyendecker, S., and Kuhl, E. (2024). Automated model discovery for human cardiac tissue: Discovering the best model and parameters. *Computer Methods in Applied Mechanics and Engineering*.

McCulloch, J., Pierre, S. S., Linka, K., and Kuhl, E. (2024). On sparse regression, lp-regularization, and automated model discovery. *International Journal for Numerical Methods in Engineering*.

Nikolov, D. P., Srivastava, S., Abeid, B. A., Scheven, U. M., Arruda, E. M., Garikipati, K., and Estrada, J. B. (2022). Ogden material calibration via magnetic resonance cartography, parameter sensitivity and variational system identification. *Philosophical Transactions of the Royal Society A: Mathematical, Physical and Engineering Sciences*.

Peirlinck, M., Costabal, F. S., Sack, K. L., Choy, J. S., Kassab, G. S., Guccione, J. M., Beule, M. D., Segers, P., and Kuhl, E. (2019). Using machine learning to characterize heart failure across the scales. *Biomechanics and Modeling in Mechanobiology*.

Peirlinck, M., Hurtado, J. A., Rausch, M. K., Tepole, A. B., and Kuhl, E. (2024a). A universal material model subroutine for soft matter systems. *Engineering with Computers*.

Peirlinck, M., Linka, K., Costabal, F. S., Bhattacharya, J., Bendavid, E., Ioannidis, J. P. A., and Kuhl, E. (2020). Visualizing the invisible: The effect of asymptomatic transmission on the outbreak dynamics of covid-19. *Computer Methods in Applied Mechanics and Engineering*.

Peirlinck, M., Linka, K., Hurtado, J. A., Holzapfel, G. A., and Kuhl, E. (2024b). Democratizing biomedical simulation through automated model discovery and a universal material subroutine. *Computational Mechanics*.

Peirlinck, M., Linka, K., Hurtado, J. A., and Kuhl, E. (2024c). On automated model discovery and a universal material subroutine for hyperelastic materials. *Computer Methods in Applied Mechanics and Engineering*.

Peng, G. C. Y., Alber, M., Tepole, A. B., Cannon, W. R., De, S., Dura-Bernal, S., Garikipati, K., Karniadakis, G., Lytton, W. W., Perdikaris, P., Petzold, L., and Kuhl, E. (2021). Multiscale modeling meets machine learning: What can we learn? *Archives of Computational Methods in Engineering*.

Pierre, S. R. S., Linka, K., and Kuhl, E. (2023). Principal-stretch-based constitutive neural networks autonomously discover a subclass of ogden models for human brain tissue. *Brain Multiphysics*.

Sommer, G., Schriefl, A. J., Andrä, M., Sacherer, M., Viertler, C., Wolinski, H., and Holzapfel, G. A. (2015). Biomechanical properties and microstructure of human ventricular myocardium. *Acta Biomaterialia*.

Taç, V., Linka, K., Sahli-Costabal, F., Kuhl, E., and Tepole, A. B. (2024). Benchmarking physics-informed frameworks for data-driven hyperelasticity. *Computational Mechanics*.